Available online at www.sciencedirect.com

ScienceDirect

Journal of Magnesium and Alloys 12 (2024) 2447–2461

www.elsevier.com/locate/jma

Full Length Article

The effect of Laves phases and nano-precipitates on the electrochemical corrosion resistance of Mg-Al-Ca alloys under alkaline conditions

Markus Felten[a], Veronika Chaineux[a], Siyuan Zhang[b], Ali Tehranchi[b], Tilmann Hickel[b], Christina Scheu[b], Joshua Spille[c], Marta Lipińska-Chwałek[d], Joachim Mayer[c,d], Benjamin Berkels[e], Marcus Hans[f], Imke Greving[g], Silja Flenner[g], Sandra Sefa[g], Daniela Zander[a,*]

[a] *Chair of Corrosion and Corrosion Protection, RWTH Aachen University, Aachen 52072 Germany*
[b] *Max-Planck-Institut für Eisenforschung GmbH, Düsseldorf 40237 Germany*
[c] *Central Facility for Electron Microscopy, RWTH Aachen University, Aachen 52074 Germany*
[d] *Ernst Ruska-Centre for Microscopy and Spectroscopy with Electrons, Forschungszentrum Jülich GmbH, Jülich 52428, Germany*
[e] *Mathematical Image and Signal Processing, Aachen Institute for Advanced Study in Computational Engineering Science, RWTH Aachen University, Aachen 52062 Germany*
[f] *Materials Chemistry, RWTH Aachen University, Aachen 52074 Germany*
[g] *Institute of Materials Physics, Helmholtz-Zentrum Hereon, Geesthacht 21502 Germany*

Received 25 April 2024; received in revised form 29 May 2024; accepted 12 June 2024
Available online 27 June 2024

Abstract

The electrochemical corrosion mechanisms of Mg alloys were extensively studied in previous investigations of different chemical compositions, modified surface states and various electrolyte conditions. However, recent research focused on the active state of Mg dissolution, leading to unresolved effects of secondary phases adjacent to a stable α-solid solution passive layer. The present study investigates the fundamental electrochemical corrosion mechanisms of three different Laves phases with varying phase morphologies and phase fractions in the passive state of Mg-Al-Ca alloys. The microstructure was characterized by (transmission-) electron microscopy and synchrotron-based transmission X-ray microscopy. The electrochemical corrosion resistance was determined with a standard three-electrode setup and advanced in-situ flow cell measurements. A new electrochemical activity sequence (C15>C36>α-Mg>C14) was obtained, as a result of a stable passive layer formation on the α-solid solution. Furthermore, nm-scale Mg-rich precipitates were identified within the Laves phases, which tend to inhibit the corrosion kinetics.

Keywords: Laves phase; STEM; Magnesium; Corrosion; Passive layer.

---

1. Introduction

The global effort to reduce the human CO_2 footprint towards a sustainable economy illustrates the urgent requirement of cost-efficient lightweight materials, which might consequently substitute long-term established alloys. Thus, magnesium (Mg) with a density of 1.74 g/cm^3 and Mg alloys represent a crucial material class for various applications in the medical [1-3] or aerospace [4-6] sector and as a potential anode material in air batteries [7-9]. While Mg-Al-Zn alloys were extensively studied in terms of their mechanical [10-12] and electrochemical [13-15] properties, recent research focuses on Mg-Al-Ca alloys as well [16-19]. Mg-Al-Ca alloys exhibit excellent mechanical properties at elevated temperatures ($T > 150$ °C) due to microstructural inherent intermetallic Laves phases [20-22]. Depending on the nominal Ca/Al ratio, either Mg_2Ca (C14), $(Mg,Al)_2Ca$ (C36) or Al_2Ca

---

[*] Corresponding author.
E-mail address: d.zander@gi.rwth-aachen.de (D. Zander).

https://doi.org/10.1016/j.jma.2024.06.011

(C15) are thermodynamically predicted [23,24] and were experimentally observed [25-27] in the as cast condition. Zubair et al. [18] further conducted a heat treatment of Mg-Al-Ca alloys and observed both a C36 to C15 solid-state transformation and a secondary phase morphology modification from an interconnected skeleton to finely dispersed spherical particles.

The high chemical activity of Mg combined with a merely partially protective surface film formed in aqueous electrolytes generally limits the widespread application of Mg alloys [28-30]. The native oxide on Mg comprises an inner MgO layer beneath a thin $Mg(OH)_2$ layer [31-35]. The oxide/hydroxide film formed in neutral aqueous electrolytes was instead either described as an inner hydrated $Mg(OH)_2$ layer with an intermediate MgO layer [36] or a nanocrystalline $MgO/Mg(OH)_2$ mixture [37] beneath an outer plate-like $Mg(OH)_2$ layer. For Mg-Al alloys a further Al enriched Mg/MgO interface was experimentally observed [38] and theoretically predicted via surface phase diagrams by Yang et al. [39]. Nordlien et al. [38] observed a maximum Al/Mg weight ratio of 35% at the Mg/MgO interface after exceeding the Mg-Al solid solution threshold of $c_{Al}>4$ wt.%, leading to a continuous skeletal Al enriched barrier that improves the electrochemical corrosion resistance. Furthermore, Ca tends to reduce the cathodic as well as the anodic partial reaction due to an oxide/hydroxide layer reinforcement via Ca or $CaCO_3$ [40]. The oxide/hydroxide formation was extensively studied under neutral immersion conditions, while fewer studies focused on alkaline electrolytes with $pH>10.5$, where $Mg(OH)_2$ is thermodynamically stable [31,41,42]. Short-term immersion experiments conducted by Felten et al. [41] under alkaline conditions (pH=11.5) on Mg-Al-Ca solid solution revealed a dense $Mg(OH)_2$ layer ($Mg(OH)_{2\_dense}$) beneath a plate-like $Mg(OH)_2$ layer ($Mg(OH)_{2\_flake}$) as the formed corrosion products. Furthermore, two Al enriched layers at the $Mg/Mg(OH)_{2\_dense}$ and the $Mg(OH)_{2\_dense}/Mg(OH)_{2\_flake}$ interfaces were observed. While the anodic partial reaction occurs across an intact oxide/hydroxide film with a valence of $n = 2$ [43-46], the cathodic partial reaction was generally believed to comprise predominantly of the hydrogen evolution reaction (HER) [47-49]. Nevertheless, recent studies exhibit a significant contribution of the oxygen reduction reaction (ORR) to the total cathodic partial reaction for ultra-high purity Mg in neutral electrolytes and Mg-Al-Ca solid solutions in alkaline electrolytes [41,50-52].

Beside the α-solid solution composition and the oxide/hydroxide structure, the microstructural inherent secondary phases affect the electrochemical corrosion resistance of varying Mg alloys [53-55]. For Mg-Al-Ca alloys in electrolytes with $pH<10.5$, a dualistic effect for the intermetallic $Mg_{17}Al_{12}$ phase and the Al_2Ca Laves phase was observed [16,56-59]. Both cathodic phases might either act as a corrosion barrier or a corrosion accelerator for the Mg dissolution, if they are continuously or discontinuously distributed within the microstructure [16,57-59]. An opposing effect was reported for the anodic Mg_2Ca Laves phase. On the one hand, the Mg_2Ca Laves phase acts as a sacrificial anode in the micro-galvanic coupling with the adjacent α-solid solution and decreases the overall corrosion current density [57]. This was observed in alloys with Mg_2Ca Laves phases in low fractions dispersed as particles. On the other hand, the Mg_2Ca Laves phase increases the corrosion current density, when the phase fraction is high enough to form a continuous and interconnected secondary phase skeleton [60-62]. The $(Mg,Al)_2Ca$ Laves phase was either described as the anode [60] or as the cathode [31,57,61,63,64] in the micro-galvanic coupling with the adjacent α-solid solution.

Nevertheless, the effect of microstructural inherent secondary phases adjacent to an α-solid solution passive layer formation on the electrochemical corrosion mechanisms has not yet been extensively analyzed in the literature. In the present study, we investigate three different Mg-Al-Ca alloys in the as cast and in a heat-treated condition, to explore this effect for the wide variety of different inherent secondary phases (C14, C36, C15), phase morphologies and phase fractions, while simultaneously obtaining comparable chemical compositions of the α-solid solutions. The microstructure was analyzed in 2D via scanning (transmission-) electron microscopy (SEM/STEM) and in 3D via synchrotron radiation-based transmission X-ray microscopy (TXM). In particular, this study focusses on the microstructure of the inherent Laves phases and the formation of nm-scale Mg-rich precipitates therein. The electrochemical corrosion resistance of the three Mg-Al-Ca alloys under alkaline immersion conditions with pH=11.5 was determined and will be discussed in detail. The alkaline electrolyte was selected to stabilize the passive layer on the α-solid solution without any film breakdown effects, to subsequently explore the fundamental electrochemical mechanisms adjacent to the different secondary phases.

2. Material and methods

2.1. Material preparation

Different Mg-Al-Ca alloys were cast in an induction furnace and subsequently solidified in a steel crucible under Ar protective gas. The chemical compositions of the Mg-Al-Ca alloys determined with inductively coupled plasma optical emission spectroscopy (ICP-OES) and mass spectrometry (ICP-MS) are listed in Table 1. Several as-cast (AX_{ac}) alloys were further annealed (AX_{ht}) under a protective Ar atmosphere at 500 °C for 48 h and cooled down with a cooling rate of ~100 °C/h. The specimens were prepared according to [65] including a first grinding step using SiC abrasive paper with a grit size of #1000 and water as a lubricant, followed

Table 1
Chemical composition of the Mg-Al-Ca alloys determined with ICP-OES and ICP-MS.

	Mg [wt.%]	Al [wt.%]	Ca [wt.%]	Fe [ppm]	Cu [ppm]	Mn [ppm]	Ni [ppm]	Si [ppm]
AX44	Bal.	3.94	3.83	20 ± 2	< 20	< 20	< 20	< 20
AX53	Bal.	4.65	2.82	11 ± 3	< 20	< 20	< 20	< 20
AX62	Bal.	5.53	1.74	39 ± 9	< 20	< 20	< 20	< 20

by a grinding procedure with a SiC paper with a grit size of #4000 and iso-propanol (Schmitz-Metallographie GmbH, Herzogenrath, Germany) as a lubricant. Afterwards, all specimens were polished with water-free 3 µm and 1 µm diamond suspension (Schmitz-Metallographie GmbH, Herzogenrath, Germany) using a DP Lubricant Blue (Struers GmbH, Willich, Germany). The final polishing step was conducted with a 0.2 µm water-free fumed silica suspension (Cloeren Technology GmbH, Wegberg, Germany) and a subsequent cleaning procedure in an ultrasonic bath with iso-propanol. Thereafter, all specimens were stored for ~24 h under moderate atmospheric conditions with a humidity of 30–40 % and a temperature of 23–25 °C to establish stable native oxide surface conditions for subsequent reliable electrochemical measurements as recommended in [31,66].

2.2. Microstructure and surface analysis

The microstructure was investigated with a Supra 55VP SEM (Carl Zeiss AG, Oberkochen, Germany) equipped with an Ultim®Max detector (Oxford Instruments plc, Abingdon, UK) for energy dispersive X-ray spectroscopy (EDS). The SEM was operated at an acceleration voltage of 10 kV. The acquired back scattered electron (BSE) images were further analyzed with an isodata algorithm [67] based threshold to automatically determine the corresponding secondary phase fractions. STEM investigations were performed on two C_s-corrected Titan microscopes (Thermo Fisher Scientific, Waltham, USA) operated at 300 kV (Titan Themis) and 200 kV (Titan G2 80–200 ChemiSTEM [68]). STEM-EDS spectrum images were acquired using the 4-quadrant SuperX detectors and multivariate statistical analysis [69] was applied to denoise various datasets. Thin lamellas for STEM investigations were prepared using focused ion beam (FIB) platforms: Scios2 and Helios NanoLab 400S (Thermo Fisher Scientific, Waltham, USA). Additional C marker was applied on the specimen surfaces to preserve the corrosion products [70].

2.3. Synchrotron-based TXM

For the TXM investigation, site-specific extraction of cylinders with a diameter of 20 µm and a length of 150 µm from each Mg-Al-Ca alloy was done with a Helios 5 Hydra UX dual-beam microscope (Thermo Fisher Scientific, Waltham, USA). FIB techniques were employed with a Xe^+ plasma source for the lift-out and preparation of the cylinders. The TXM measurement was performed at the P05 imaging beamline [71] operated by the Helmholtz-Zentrum Hereon at the PETRA III storage ring of the German Electron Synchrotron (DESY). A full-field TXM setup, equipped with a Fresnel Zone Plate of 130 µm diameter and a beam shaping optics were used for acquiring the tomograms at an energy of 11 keV in Zernike phase contrast mode. These optics were designed and manufactured at the Paul Scherrer Institute. An X-ray sCMOS camera (Hamamatsu C12849−101U, 6.5 µm pixel size, 2048 × 2048 pixel, 16-bit image depth) with a 10 µm Gadox scintillator was used as a detector. The high-resolution scanning resulted in 2D images with 15.15 nm^2 pixel size. The raw image data were reconstructed using the P05 reconstruction pipeline based on TomoPy [72] with a binning factor of two, resulting in 3D image data with a voxel size of 30.3 nm^3. The acquired images were subsequently filtered to remove textural noise using iterative non-local mean filter [73] then segmented, analyzed and visualized with the VG-Studio Max (Volume Graphics, Heidelberg, Germany) software.

2.4. Electrochemical analysis

An alkaline KOH solution (c_{KOH}=0.0032 mol/l) Roti®Metic 99.98% (Carl Roth GmbH, Karlsruhe, Germany) with a constant temperature of 25 °C and pH=11.5 ± 0.1 served as the electrolyte for all conducted electrochemical measurements. A standard three-electrode setup was utilized, which consisted of a Hg/HgO reference electrode, a platinum sheet as the counter electrode and the Mg-Al-Ca alloys with a specimen surface of 0.28 cm^2 as the working electrode. A Reference 600^{TM} (Gamry instruments, Warmister, USA) potentiostat was used. Open circuit potential (OCP) measurements were conducted for 60 min in an electrolyte volume of 750 ml. Thereafter, both hybrid electrochemical impedance spectroscopy (EIS) and potentiodynamic polarization (PDP) measurements were conducted. For EIS measurements an initial frequency of 10 kHz, a final frequency of 0.1 Hz and an applied AC voltage of 10 mV were used. PDP measurements were conducted with a scan rate of 0.8 mV/s in a potential range of −300 to 500 mV relative to the OCP. The standard electrochemical measurements were supplemented by separate flow cell experiments coupled with an ICP-MS analysis, to enable an in-situ and element specific determination of the corrosion currents. A custom-built micro-flow cell design was utilized with a specimen area of 0.03 cm^2 and a flow rate of 30 ml/h in conjunction with a NexION® 2000 ICP-MS (Perkin Elmer, Massachusetts, USA). The ICP-MS was used in the kinetic energy discrimination (KED) mode with Ar (99.999 vol%) as the nebulizer gas and He (99.9999 vol%) as the collision gas.

3. Results

3.1. Microstructural characterization

The microstructure of Mg-Al-Ca alloys depends on the chemical composition of the alloys as well as on their heat treatment [23,25-27]. Fig. 1 compares structures of the investigated Mg-Al-Ca alloys in the as-cast and the heat-treated state. Each of the alloys contain the α-solid solution and Laves phases (C14-, C15- and/or C36) coexisting as the microstructure inherent phases (Table 2), consistent with previous studies on the same material [18]. The Al content within the α-solid solution increases with the overall alloy Al concentration. The Al concentration ranges between 1.3 ± 0.4 at.% and 2.8 ± 0.6 at.% for the as-cast as well as 0.7 ± 0.0

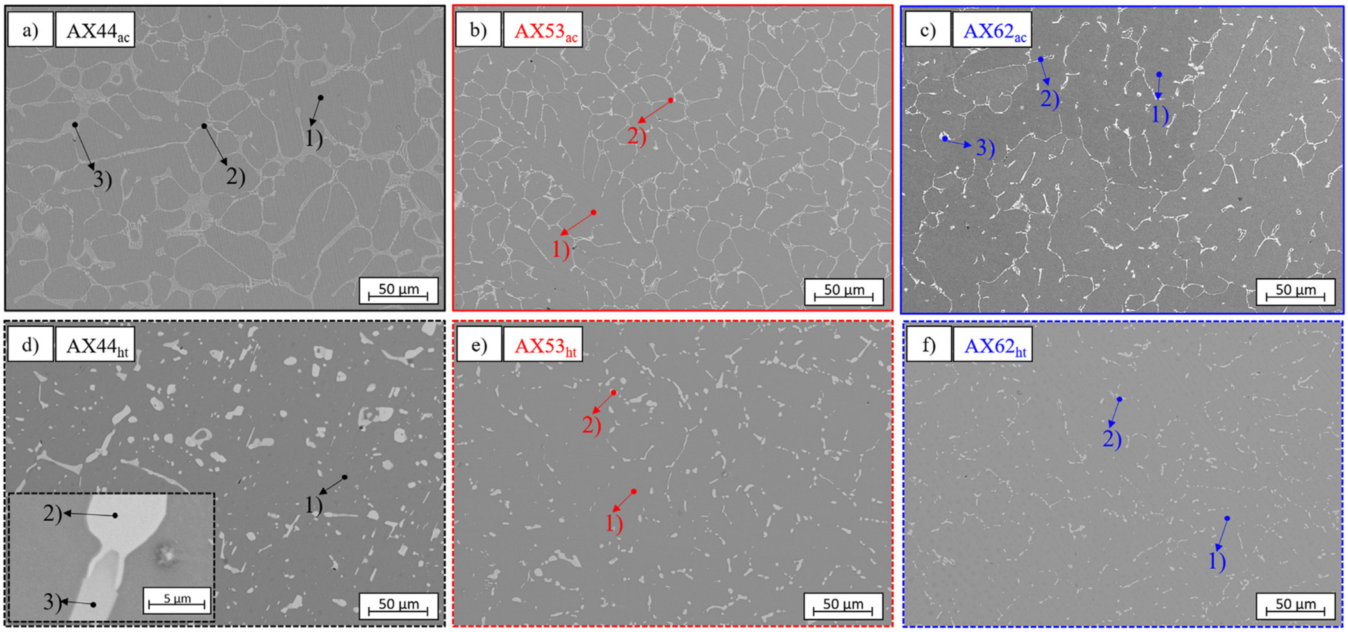

Fig. 1. SEM-BSE images of the investigated Mg-Al-Ca alloys in the as-cast and the heat-treated conditions.

Table 2
Averaged SEM-EDS spectra of the microstructure inherent phases with representative locations indicated by arrows in Fig. 1.

	Ca/Al [at.-%/ at.-%]	Al [at.-%]	Ca [at.-%]	Mg [at.-%]	Phase [-]
$AX44_{ac}$	0.65				
1)		1.3 ± 0.4	0.2 ± 0.1	98.5 ± 0.4	α-Mg
2)		40.8 ± 2.0	26.8 ± 1.3	32.4 ± 3.2	$(Mg,Al)_2Ca$
3)		13.5 ± 2.0	14.3 ± 2.3	72.2 ± 4.2	Mg_2Ca
$AX53_{ac}$	0.41				
1)		1.7 ± 0.1	0.1 ± 0.0	98.2 ± 0.2	α-Mg
2)		41.8 ± 2.1	24.5 ± 2.4	33.7 ± 4.3	$(Mg,Al)_2Ca$
$AX62_{ac}$	0.21				
1)		2.8 ± 0.6	0.1 ± 0.0	97.1 ± 0.6	α-Mg
2)		52.1 ± 3.0	24.0 ± 1.5	23.5 ± 3.6	$(Mg,Al)_2Ca$
3)		59.7 ± 0.8	25.3 ± 0.4	15.0 ± 1.2	Al_2Ca
$AX44_{ht}$	0.65				
1)		0.7 ± 0.0	0.0 ± 0.0	99.3 ± 0.0	α-Mg
2)		46.5 ± 3.3	30.1 ± 1.8	23.4 ± 5.1	$(Mg,Al)_2Ca$
3)		22.0 ± 1.3	26.7 ± 0.9	51.4 ± 2.2	Mg_2Ca
$AX53_{ht}$	0.41				
1)		1.2 ± 0.1	0.0 ± 0.0	98.8 ± 0.1	α-Mg
2)		59.4 ± 3.4	29.6 ± 1.9	11.0 ± 5.3	Al_2Ca
$AX62_{ht}$	0.21				
1)		3.1 ± 0.0	0.0 ± 0.0	96.9 ± 0.0	α-Mg
2)		60.2 ± 3.0	28.4 ± 1.6	11.4 ± 4.7	Al_2Ca

at.% and 3.1 ± 0.0 at.% for the heat-treated conditions, respectively. The phase fractions determined in 2D are given in Table 3. The $AX44_{ac}$ alloy exhibits both an interconnected fine lamellar C14 Laves phase and a rather coarse intermetallic C36 Laves phase (Fig. 1a). Both Laves phases are further observed with a dispersed particle morphology after the heat treatment in the $AX44_{ht}$ alloy (Fig. 1d), although a significant increase of the C36 Laves phase fraction and a decrease of the C14 Laves phase fraction was determined. The inset image in Fig. 1d) indicates that the solid-state transformation initiates at the C14/α-solid solution interface. The $AX53_{ac}$ alloy contains predominantly an interconnected C36 Laves phase skeleton (Fig. 1b), while the $AX62_{ac}$ (Fig. 1c) contains as well the C36 Laves phase and the C15 Laves phase, both characterized by a lower interconnectivity [18]. Unfortunately, the C36 and the C15 phases cannot be accurately distinguished via EDS-mappings (not shown) or the corresponding phase morphology in the $AX62_{ac}$ alloy, although EDS-mappings indicate a predominant C36 Laves phase. Accordingly, the phase fraction determined for the $AX62_{ac}$ alloy and listed in Table 3 is an overall number including both coexisting Laves phases. The $AX53_{ht}$ and the $AX62_{ht}$ alloys exhibit exclusively the C15 Laves phase dispersed within the matrix of the α-solid solution (Fig. 1e) and f)). More detailed characterization of interfaces, phase fractions and compositions of the investigated Mg-Al-Ca alloys were published previously by Zubair et al. [18].

In the present study, we went beyond 2D imaging and applied synchrotron-based TXM to investigate the 3D morphology and interconnectivity of the constituent phases. Such 3D analysis has proven to be pivotal in revealing the electrochemical corrosion mechanisms of biodegradable Mg–Ca–Zn alloys [74]. Fig. 2 shows the 3D representations of the Laves phases. The Laves phases in the $AX44_{ac}$ and the $AX53_{ac}$ alloys form a continuous 3D network, while the $AX62_{ac}$ alloy shows a reduced interconnectivity among the Laves phases, consistent with the 2D image analysis in Fig. 1. The C15 and the C36 Laves phases cannot be accurately distinguished in the $AX62_{ac}$ alloy based on the material contrast in the synchrotron-based TXM measurements. Thus, a cumulative volume phase fraction is listed in Table 3. All determined volume fractions agree well with the phase fractions determined in 2D. However, the 3D structure observed for the $AX44_{ht}$

Table 3
2D/3D phase fractions determined via BSE images and synchrotron-based TXM.

	$AX44_{ac}$	$AX53_{ac}$	$AX62_{ac}$	$AX44_{ht}$	$AX53_{ht}$	$AX62_{ht}$
2D						
C14 [%]	9.7 ± 0.8	-	-	3.2 ± 0.5	-	-
C36 [%]	1.1 ± 0.7	6.7 ± 0.8	4.4 ± 0.4	4.4 ± 0.1	-	-
C15 [%]	-	-		-	4.8 ± 0.4	3.3 ± 0.1
3D						
C14 [%]	9.7	-	-	7.1	-	-
C36 [%]	0.8	6.5	3.6	4.1	-	-
C15 [%]	-	-		-	4.4	2.8

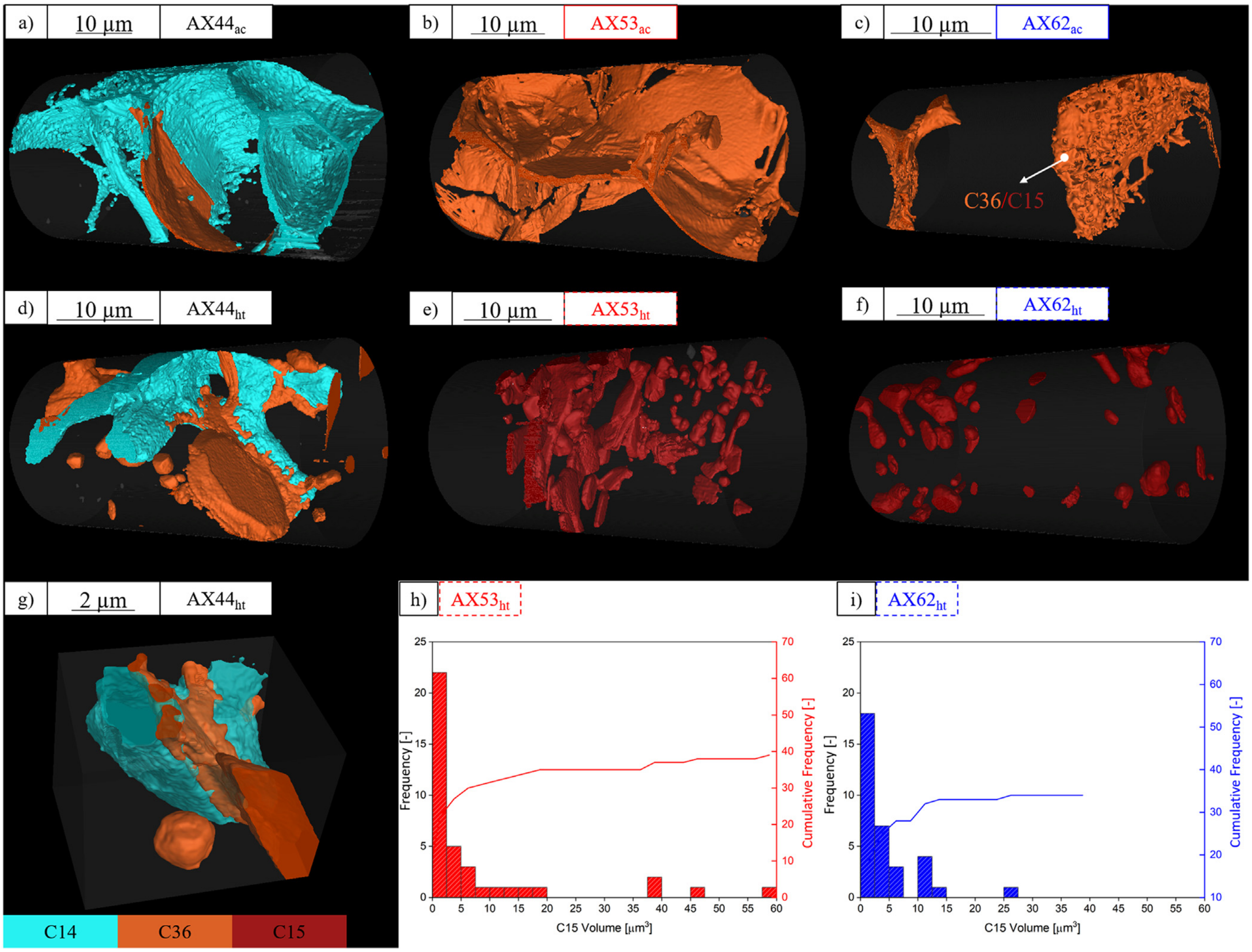

Fig. 2. a-g) 3D representation of the Laves phase morphologies within the Mg-Al-Ca alloys acquired with the synchrotron-based TXM measurements. h,i) particle volume distribution of the C15 Laves phases in the heat-treated $AX53_{ht}$ and $AX62_{ht}$ alloys.

alloy in Fig. 2d) reveals an interconnected C36/C14 Laves phase network, while the 2D analysis in Fig. 1d) indicated the presence of merely disconnected spherical Laves phases. Thus, the 3D microstructure analysis more accurately reflects the interconnectivity of the precipitated phases. Furthermore, 3D analysis of the microstructure for the $AX44_{ht}$ alloy (Fig. 2g) confirms our findings derived from the corresponding 2D analysis, that the C14 to C36 solid-state transformation initiates from the C14/α-solid solution interface. Accordingly, we conclude, that the transformation proceeds preferentially at the C14/α-solid solution interface resulting in the $AX44_{ht}$ structure with C36 Laves phase surrounding the C14 Laves phase in 3D. Fig. 2e) and f) show 3D spherical dispersed C15 Laves phase particles within the $AX53_{ht}$ and the $AX62_{ht}$ alloys. The corresponding volume histograms for the Laves phase particles, analyzed in equal cylindrical volumes with a diameter of 15 µm and a length of 17 µm, are shown in Fig. 2h) and i), respectively. Although both alloys contain a

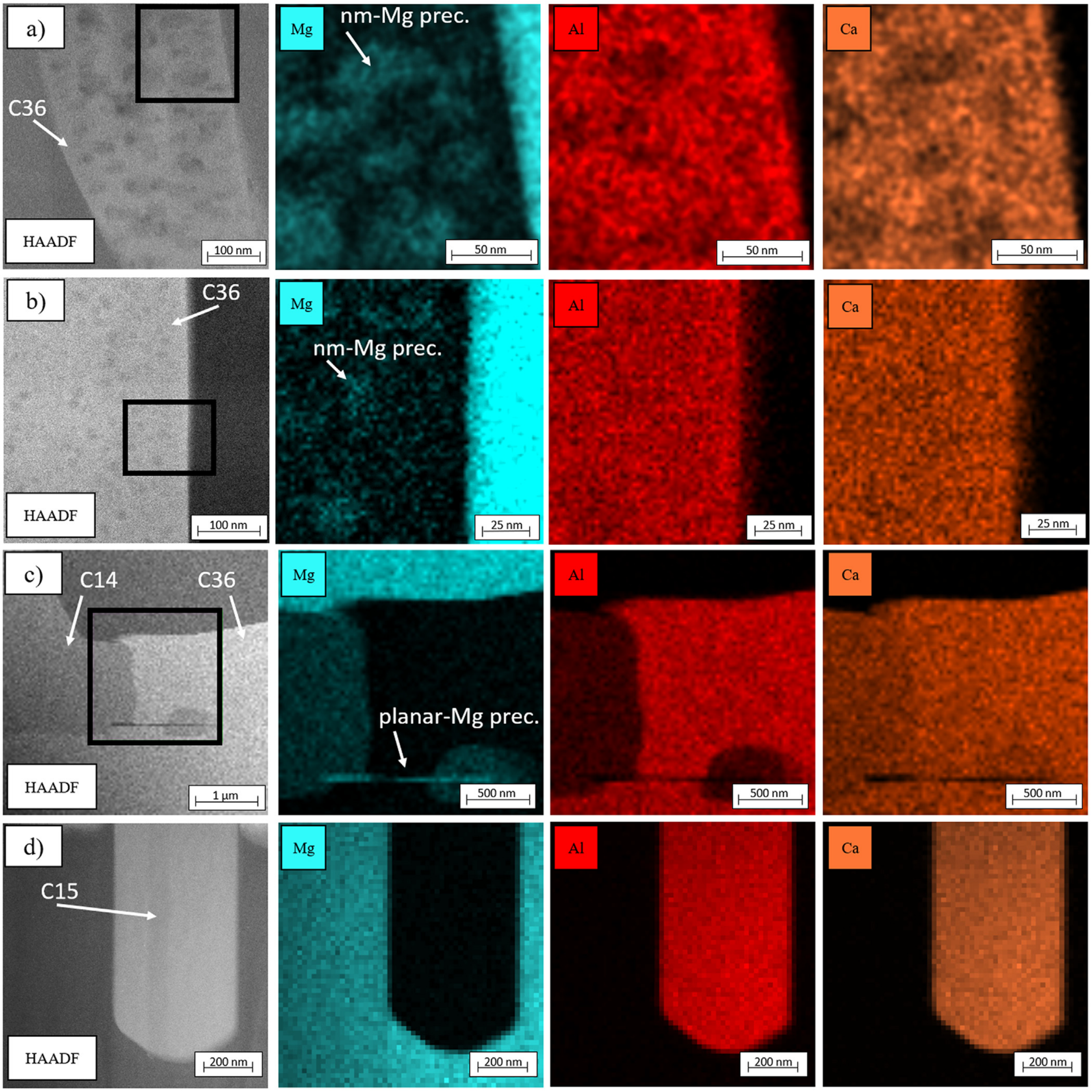

Fig. 3. STEM/EDS analysis of a) a C36 Laves phase in the $AX53_{ac}$ alloy, b) a C36 Laves phase in the $AX62_{ac}$ alloys, c) both C14- and C36 Laves phases in the $AX44_{ht}$ alloy and d) a C15 Laves phase in the $AX62_{ht}$ alloy.

comparable amount of C15 Laves phases, larger C15 particles are observed within the volume distribution for the $AX53_{ht}$ alloy.

Selected Laves phases were further investigated by STEM/EDS (Fig. 3 and Table 4), in line with previous studies on the same material [18]. Fig. 3a) presents the characteristic structure observed for the $AX53_{ac}$ alloy, consisting of a α-Mg matrix and an interconnected C36 Laves phase skeleton. A detailed analysis of the inherent Laves phase revealed the presence of homogeneously distributed nm-scale precipi-

Table 4
STEM/EDS values of the Laves phases in Fig. 3.

	Al [at.-%]	Ca [at.-%]	Mg [at.-%]
$AX53_{ac}$			
C36	58	27	15
$AX44_{ht}$			
C14	22	31	47
C36	51	32	17
$AX62_{ht}$			
C15	65	32	3

tates (Fig. 3a) and b)). The precipitates are enriched in Mg and depleted in Al and Ca compared to the surrounding C36 Laves phase. The distinct stoichiometry of these precipitates could not be unambiguously determined from FIB prepared samples due to the fine size of the Mg-enriched precipitates. Accordingly, the EDS signal acquired for the material regions containing nm-scale sized Mg-rich precipitates contains also superimposed information from the surrounding C36 Laves phase. Experiments aiming for an exact determination of the precipitate composition are currently undergoing by corelative employment of TEM and atom probe tomography (APT) measurements and will be reported in near future. Precipitates in similar dimension, distribution and chemical composition were observed in the C36 Laves phases within the $AX62_{ac}$ alloy structure image displayed in Fig. 3b), but not in the C36 or C14 Laves phases within the $AX44_{ac}$ alloy. The STEM/EDS analysis of the $AX44_{ht}$ alloy revealed the presence of larger planar precipitates, with nm-scale thickness and μm-scale lateral size, present within the C36 and the C14 Laves phases and across their interface. An example of these defects can be observed as horizontal line within the bottom part of the inset indicated in Fig. 3c). These planar precipitates are also enriched in Mg and depleted in Al and Ca compared to the adjacent Laves phases. The C15 Laves phase within the $AX62_{ht}$ alloy in Fig. 3d) does not show any precipitates.

3.2. Electrochemical analysis

Fig. 4a) exhibits the OCP of the Mg-Al-Ca alloys in the as cast condition. All investigated alloys in the as cast condition reveal an equivalent initial OCP of ~1.2 $V_{Hg/HgO}$, which subsequently increases with time. The OCP gradually turns into different dynamic equilibriums towards the final immersion time of 60 min, indicating a steady state condition with a potentially stable passive layer formation. Fig. 4b) shows the OCP of the Mg-Al-Ca alloys in the heat-treated condition. While the $AX44_{ht}$ alloy shows a similar trend as observed for the Mg-Al-Ca alloys in the as cast condition, the initial OCP of the $AX53_{ht}$ and the $AX62_{ht}$ alloys is significantly lower and does not turn into a dynamic equilibrium towards the final immersion time. Thus, the OCP of the $AX62_{ht}$ alloy reaches even a similar range like the OCP of the $AX44_{ht}$ alloy at the final immersion time. All alloys exhibit a characteristic anodic passive behavior without a film breakdown indication during anodic polarization in the representative PDP measurements in Fig. 4c) and d), which further reinforces the assumption of a stable passive layer formation. The quantitative electrochemical parameters derived from the PDP measurements are highlighted in Table 5. The $AX53_{ac}$, $AX62_{ac}$ and $AX44_{ht}$ alloys reveal the highest corrosion resistances among the investigated Mg-Al-Ca alloys, indicated by relative low corrosion current densities (i_{corr}), low passive current densities (i_{pas}) and high polarization resistances (R_p). The $AX62_{ht}$ alloy exhibits a slightly lower corrosion resistance, followed by the $AX44_{ac}$ and the $AX53_{ht}$ alloys. Interestingly, the corrosion resistance correlates with the cathodic Tafel slope (β_c). A decreasing corrosion resistance corresponds to a reduced kinetic of the cathodic partial reaction. This correlation was previously reported for Mg and Mg alloys under alkaline immersion conditions [31]. A thicker $Mg(OH)_{2\_dense}$ layer is assumed to correlate with an increasing i_{corr} and a subsequent reduced ORR contribution. This effect appears reasonable in the present study as the ORR contribution for Mg-Al-Ca solid solution under alkaline immersion conditions (pH=11.5) equals ~9 % [41].

Hybrid EIS measurements were conducted to further validate the different corrosion resistances among the investigated Mg-Al-Ca alloys. Fig. 5 shows the Nyquist-plots and the Bode-plots after an immersion time of 60 min. The Mg-Al-Ca alloys in the as cast condition and the $AX44_{ht}$ alloy exhibit a distinct high-frequency (HF) capacity loop and the onset of a low-frequency (LF) capacity loop. The HF-loop is associated with the combined effects of the charge transfer resistance in conjunction with film effects, while the LF-Loop was associated with mass transfer effects and the electrolytic resistance in film layer pores [75-78]. Baril et al. [75,76] reported that the HF-loop sufficiently represents the corrosion resistance of Mg alloys. Therefore, the equivalent electrical circuit 1) used in [31,75] and displayed in Fig. 5a) was utilized to fit the HF-loops for the Mg-Al-Ca alloys in the as cast condition and the $AX44_{ht}$ alloy. The equivalent circuit comprises the electrolyte resistance (R_s), the charge transfer resistance (R_{ct}), the film resistance (R_f), the electrochemical double layer capacity (C_{ct}) and the constant phase element for the oxide layer (CPE_f), respectively. Furthermore, a characteristic constant value of $C_{ct}=16\ \mu F/cm^2$ was assumed as determined for Mg alloys in a comparable alkaline electrolyte with pH=11.0 [78]. The CPE element impedance (Z_{CPE}) is calculated according to Eq. (1) [79], where j represents an imaginary number, ω the AC frequency, α a model parameter and Y_0 a CPE parameter. In case of $\alpha = 1$, the CPE element equals an ideal capacitor and subsequently $Y_0 = C$.

$$Z_{CPE} = \frac{1}{(j\omega)^{\alpha} Y_0} \tag{1}$$

Table 6 shows that the determined charge transfer resistance is significantly lower than the film resistance for each investigated Mg-Al-Ca alloy, which again indicates a stable passive layer formation under alkaline electrolyte conditions. The $AX53_{ht}$ and the $AX62_{ht}$ alloys exhibit a pronounced and partially overlapping LF-Loop in the Nyquist plot, corresponding to the second time constant at frequencies in the range of ~2–5 Hz. The LF-loop fit is required for both alloys, to accurate deconvolute the HF-Loop. Therefore, a CPE_{pore} in parallel with R_{pore} was used to account for the electrolytic capacity and the resistance in passive film pores. Furthermore, the charge transfer, the film resistance, the electrochemical double layer and oxide layer contributions are combined in a single Randles circuit (CPE_{ct+f} parallel to R_{ct+f}) to model a simplified HF-loop in the equivalent electrical circuit 2) displayed in Fig. 5d). For all alloys $R_{ct}+R_f$ in Table 6 represents the overall corrosion resistance according to [75,76]. The $AX53_{ac}$ alloy reveals the highest corrosion

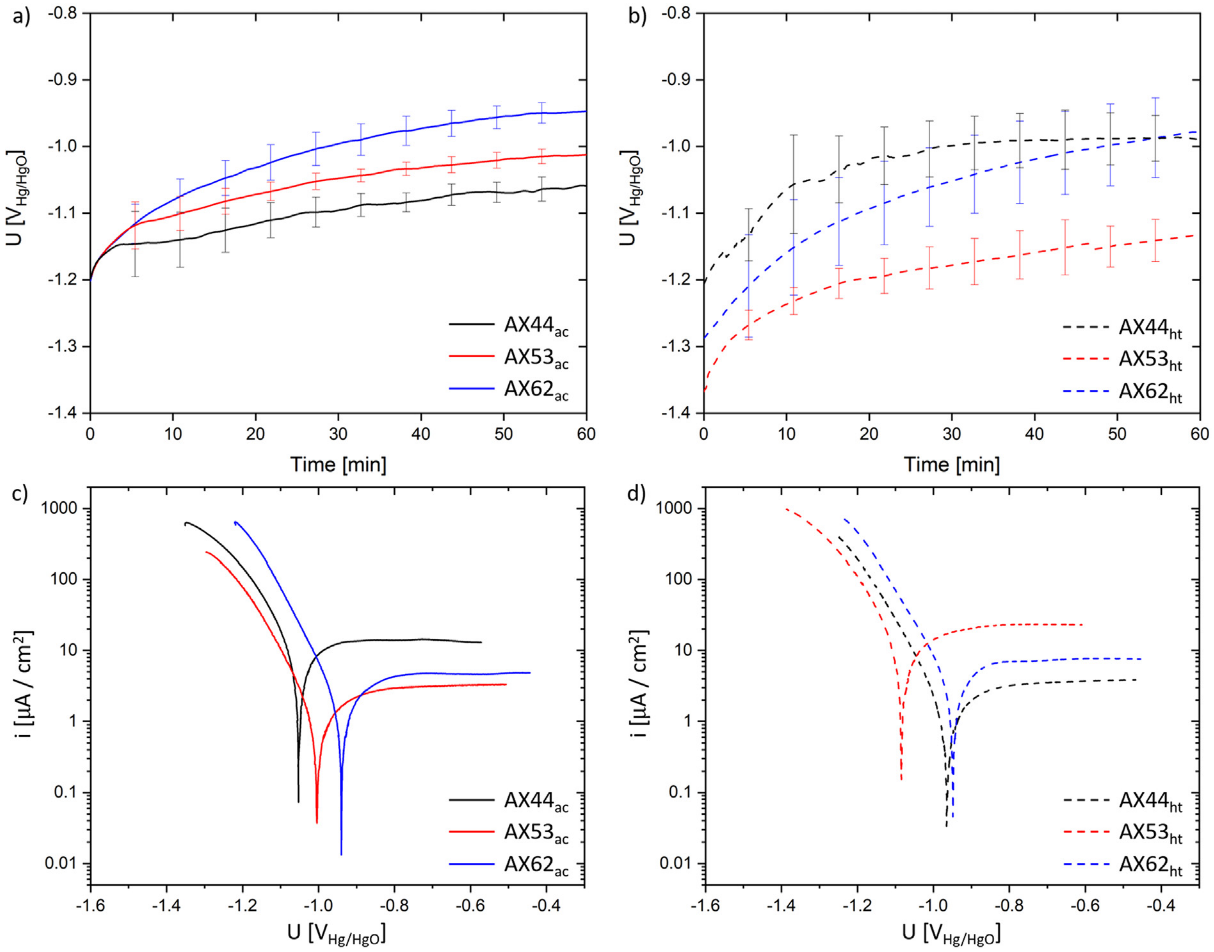

Fig. 4. a,b) Averaged OCP and c,d) representative PDP measurements for the Mg-Al-Ca alloys after 60 min immersion in a KOH electrolyte (pH=11.5 ± 0.1).

Table 5
Open Circuit Potential (U_{OCP}), corrosion potential (U_{corr}), corrosion current density (i_{corr}), polarization resistance (R_p), passive current density (i_{pas}), cathodic Tafel slope (β_c) derived from the PDP measurements for the Mg-Al-Ca alloys after 60 min immersion in a KOH electrolyte (pH=11.5 ± 0.1).

	U_{OCP} [$V_{Hg/HgO}$]	U_{corr} [$V_{Hg/HgO}$]	i_{corr} [μAcm^{-2}]	R_p [$k\Omega\ cm^2$]	i_{pas} [μAcm^{-2}]	β_c [$V\ dec^{-1}$]
$AX44_{ac}$	−1.06 ± 0.02	−1.04 ± 0.02	7.1 ± 2.3	5 ± 2	11.0 ± 2.1	−0.107 ± 0.005
$AX53_{ac}$	−1.01 ± 0.01	−1.00 ± 0.01	1.2 ± 0.3	20 ± 3	3.5 ± 0.5	−0.099 ± 0.002
$AX62_{ac}$	−0.95 ± 0.02	−0.94 ± 0.01	1.4 ± 0.4	17 ± 4	4.3 ± 0.8	−0.099 ± 0.006
$AX44_{ht}$	−1.01 ± 0.04	−0.97 ± 0.02	1.4 ± 0.3	17 ± 4	4.0 ± 0.6	−0.099 ± 0.001
$AX53_{ht}$	−1.12 ± 0.03	−1.11 ± 0.03	13.3 ± 2.4	3 ± 0.4	24.2 ± 3.7	−0.120 ± 0.004
$AX62_{ht}$	−0.97 ± 0.04	−0.97 ± 0.06	3.3 ± 1.2	8 ± 1	7.4 ± 0.8	−0.103 ± 0.011

resistance among the investigated alloys. The $AX62_{ac}$ and the $AX44_{ht}$ alloys exhibit a slightly lower corrosion resistance, followed by the $AX62_{ht}$ alloy. The $AX44_{ac}$ and the $AX53_{ht}$ alloys show even lower corrosion resistances. The hybrid EIS fitting results thus reveal a similar corrosion resistance for the investigated Mg-Al-Ca alloys as already determined in the PDP measurements.

However, both the EIS and the PDP results represent the electrochemical corrosion properties exclusively at the immersion time of 60 min and they could not distinguish the different alloying elements. Therefore, flow cell experiments coupled with an ICP-MS analysis were performed, which enable the in-situ observation of dissolving elemental species “s” (s=Mg,Al,Ca) from the Mg-Al-Ca alloys in the electrolyte and the subsequent calculation of the element specific corrosion current densities (i_s) via Faraday’s law. Fig. 6 shows the calculated in-situ and element specific corrosion current densities of each investigated Mg-Al-Ca alloy. All alloys exhibit a decreasing dissolution tendency, which reinforces the notion of a stable oxide/hydroxide layer formation. The $AX62_{ac}$, the $AX62_{ht}$ and the $AX53_{ht}$ alloys show a pronounced initial and subsequently decreasing i_{Al}, which reaches a steady state for the $AX62_{ac}$ and the $AX62_{ht}$ alloys towards the final immersion time. The $AX44_{ac}$ alloy instead exhibits $i_{Mg,Ca}$ as the

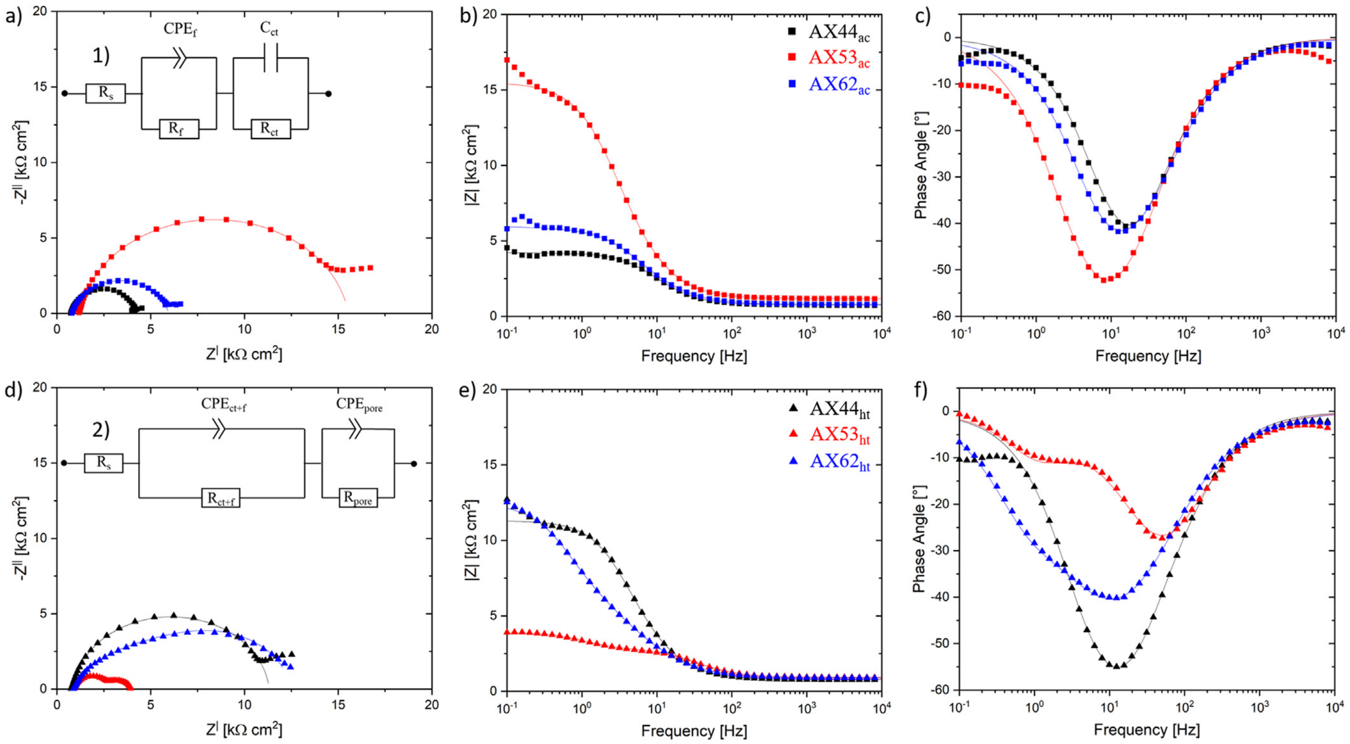

Fig. 5. Representative Nyquist-plots and Bode plots after 60 min immersion of the Mg-Al-Ca alloys in a KOH electrolyte (pH=11.5 ± 0.1) with the corresponding equivalent electrical circuits and the fitting curves.

Table 6
Fitting results of the EIS measurements after 60 min immersion of the Mg-Al-Ca alloys in a KOH electrolyte (pH=11.5 ± 0.1).

	$AX44_{ac}$	$AX53_{ac}$	$AX62_{ac}$	$AX44_{ht}$	$AX53_{ht}$	$AX62_{ht}$
R_s [kΩ]	3.8 ± 1.2	4.1 ± 0.3	3.3 ± 0.5	3.1 ± 0.9	3.4 ± 0.3	3.1 ± 0.6
R_{ct} [kΩ cm^2]	0.6 ± 0.7	1.4 ± 2.6	2.8 ± 0.8	0.6 ± 1.2	-	-
R_f [kΩ cm^2]	3.0 ± 1.0	12.1 ± 1.6	6.9 ± 4.9	9.1 ± 3.3	-	-
R_{ct}+ R_f [kΩ cm^2]	3.6 ± 0.6	13.4 ± 2.9	9.7 ± 5.7	9.7 ± 2.4	2.0 ± 0.2	6.3 ± 1.5
a_f [-]	0.89 ± 0.09	0.93 ± 0.02	0.80 ± 0.02	0.92 ± 0.03	-	-
Y_f [μSs^a cm^{-2}]	13.7 ± 8.8	6.7 ± 1.4	18.8 ± 2.2	7.8 ± 3.2	-	-
a_{ct+f} [-]	-	-	-	-	0.87 ± 0.02	0.92 ± 0.07
Y_{ct+f} [μSs^a cm^{-2}]	-	-	-	-	6.3 ± 0.9	38 ± 18
R_{pore} [kΩ cm^2]	-	-	-	-	1.0 ± 0.1	5.9 ± 2.8
a_{pore} [-]	-	-	-	-	1.0 ± 0.0	0.8 ± 0.1
Y_{pore} [μSs^a cm^{-2}]	-	-	-	-	155 ± 26	26 ± 19
X^2 [10^{-6}]	120 ± 145	52 ± 21	38 ± 22	100 ± 110	885 ± 578	362 ± 413

highest dissolution current densities among all investigated Mg-Al-Ca alloys throughout the entire immersion time. The $i_{Mg,Ca}$ values slightly decay up to 40 min and thereafter remain constant. The coupled Ca and Mg dissolution might arise as a consequence of an anodic C14 Laves phase dissolution, as reported for neutral electrolytes [57,60]. However, an independent i_{Al} is observed in Fig. 6a), although the C14 Laves phase comprises an Al concentration of c_{Al}~22 at.%. Thus, a rather different dissolution mechanism is assumed under alkaline immersion conditions. The $AX53_{ac}$ alloy shows

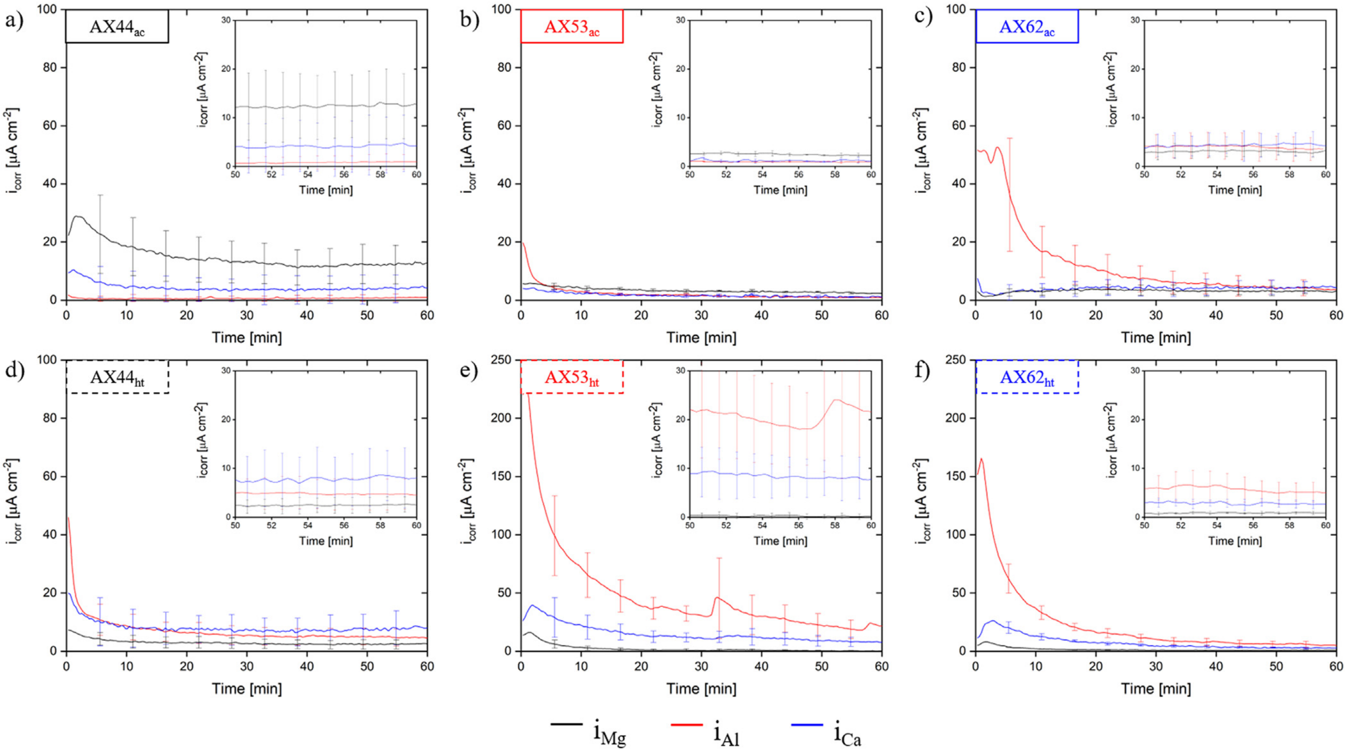

Fig. 6. In-situ ion selective corrosion current densities for the Mg-Al-Ca alloys in a KOH electrolyte (pH=11.5 ± 0.1). Note the different scale used in e) and f) for visualization.

Table 7
Averaged values of the ion selective corrosion current densities determined within an immersion time of 55–60 min from Fig. 6.

	i_{Mg} [μAcm^{-2}]	i_{Al} [μAcm^{-2}]	i_{Ca} [μAcm^{-2}]	i_{tot} [μAcm^{-2}]
$AX44_{ac}$	12.5 ± 5.6	0.9 ± 1.1	4.2 ± 4.5	17.6 ± 11.2
$AX53_{ac}$	2.5 ± 0.3	0.9 ± 0.0	1.2 ± 0.1	4.6 ± 0.4
$AX62_{ac}$	3.1 ± 0.9	4.0 ± 2.1	4.4 ± 1.8	11.5 ± 4.1
$AX44_{ht}$	2.5 ± 1.3	4.8 ± 2.6	7.9 ± 4.6	15.2 ± 8.4
$AX53_{ht}$	0.4 ± 0.3	19.5 ± 7.2	8.3 ± 3.5	28.2 ± 10.6
$AX62_{ht}$	0.9 ± 0.2	5.7 ± 2.0	2.8 ± 0.7	9.4 ± 2.8

almost constantly low $i_{Mg,Al,Ca}$ values throughout the whole immersion time. The flow cell experiments determine a similar overall corrosion resistance in Table 7 towards the final immersion time of 60 min as already observed in the PDP/EIS measurements. A significantly high corrosion resistance of the $AX53_{ac}$ alloy is observed and the $AX44_{ac}$ and the $AX53_{ht}$ alloys show the lowest corrosion resistances. The higher total elemental dissolution current densities (i_{tot}) compared to the PDP analysis might arise as a consequence of the flowing electrolyte. A flowing electrolyte could reduce the $Mg(OH)_{2\_flake}$ precipitation due to a lower local Mg^{2+} concentration and might further remove additional porous corrosion products from the surface. This effect would consequently cause an enhanced mass transport through the oxide/hydroxide and therefore lead to increased corrosion current densities. Furthermore, all species incorporated in the oxide/hydroxide layer are not detected with the ICP-MS and are therefore neglected in the element specific corrosion current density calculation. Therefore, a subsequent surface analysis is required to identify the underlying electrochemical corrosion mechanisms.

3.3. Surface analysis after corrosion

The oxide/hydroxide formed on the α-solid solution after the final immersion time of 60 min in the stagnant KOH electrolyte (pH=11.5 ± 0.1) was investigated for the $AX53_{ac}$ alloy by STEM-EDS. Fig. 7 presents the HAADF image of the surface structure formed at the α-solid solution surface, together with the corresponding chemical elements distributions across the distinct oxide/hydroxide structures, as measured with EDS along the lines indicated with the arrows 1 and 2. Our observations are in line with the previously reported findings in [41]: The hydroxide structure comprises a ~30 nm thick outer flake like $Mg(OH)_2$ layer ($Mg(OH)_{2\_flake}$) located above a ~20 nm thick inner dense $Mg(OH)_2$ layer ($Mg(OH)_{2\_dense}$). The $Mg(OH)_{2\_flake}$ layer exhibits a porous structure after precipitating from the electrolyte [36] and contains a small amount of both Ca and Al. The $Mg(OH)_{2\_dense}$ layer forms as a thermodynamic stable passive layer during the electrochemical Mg corrosion [42]. The corresponding elemental distribution was measured by EDS in the position indicated with arrow 2 and reveals the presence of two discontinuous Al enriched (~10 nm thick) interfaces: $Mg/Mg(OH)_{2\_dense}$ and $Mg(OH)_{2\_dense}/Mg(OH)_{2\_flake}$. While the Al enrichment at the $Mg(OH)_{2\_dense}/Mg(OH)_{2\_flake}$

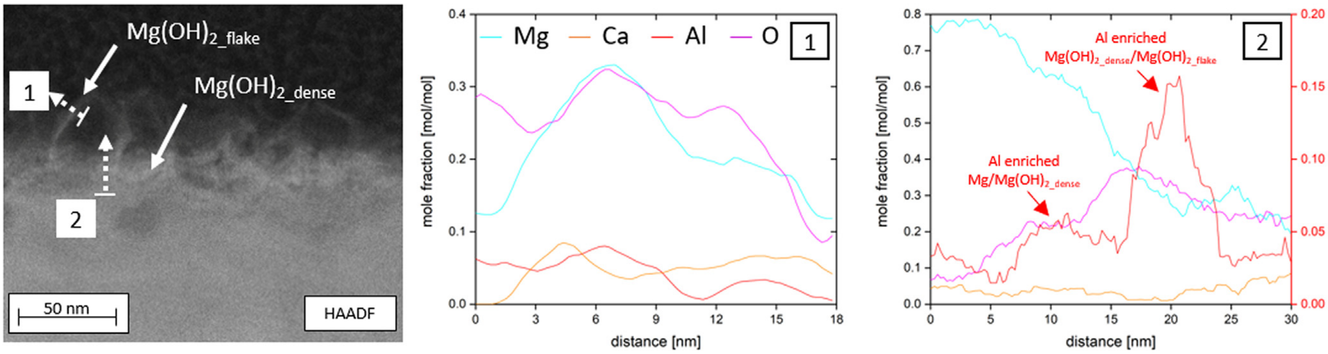

Fig. 7. STEM-EDS analysis of the α-solid solution for the $AX53_{ac}$ alloy after an immersion time of 60 min in a KOH electrolyte (pH=11.5 ± 0.1).

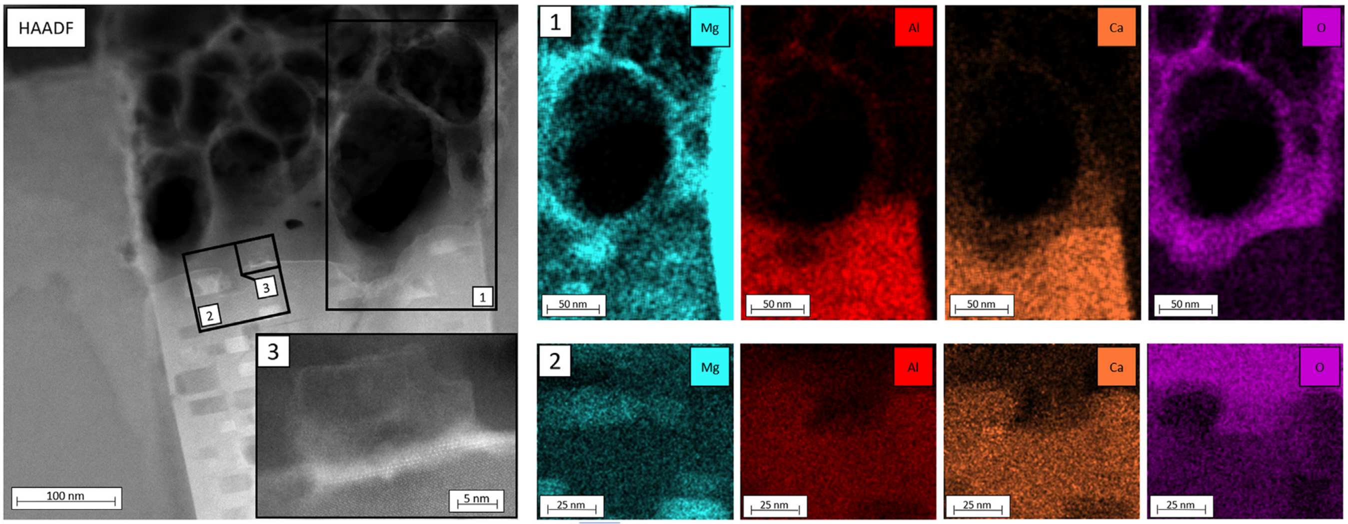

Fig. 8. STEM-EDS analysis of a C36 Laves phase in the $AX53_{ac}$ alloy after a final immersion time of 60 min in a KOH electrolyte (pH=11.5 ± 0.1).

interface stems from the native oxide [41], we associate the Al enrichment at the $Mg/Mg(OH)_{2\_dense}$ interface with an increasing corrosion resistance in various electrolytes, as previously reported in [38,80,81]. Since Al does not form oxides or hydroxides in electrolytes with pH=11.5 [42], the Al stability of both interfaces was assumed in [41] to exhibit a similar stability as the Al monolayer layer predicted via DFT-based surface phase diagrams at the Mg/MgO interface [39].

The electrochemical corrosion properties of Mg-Al-Ca alloys are further affected by the microstructural inherent Laves phases [53-55]. An anodic C36 Laves phase dissolution with a penetration depth of l_{pd}~200 nm adjacent to a cathodic α-solid solution (l_{pd}~20 nm) is observed in the $AX53_{ac}$ alloy (Fig. 8). The STEM-EDS analysis at the C36/corrosion front interface reveals a spatially varying composition of $\sim Mg_{35}Al_{50}Ca_{15}$ on the C36 Laves phase. Fig. 8 exhibits a delayed dissolution of the nm-scale Mg-rich precipitates compared to the C36 Laves phase. The delayed dissolution might arise as a consequence of the increased Mg concentration, which leads to a local stable passive layer formation under alkaline immersion conditions similar to the $Mg(OH)_{2\_dense}$ layer formed on the α-solid solution. Nevertheless, the corrosion path propagates predominantly between the nm-scale Mg-rich precipitates and will therefore physically disconnects these phases from the C36 Laves phase, leading to a subsequent electrochemical dissolution.

Fig. 9a) and b) show the C36 Laves phase dissolution with inherent nm-scale Mg-rich precipitates in both the $AX53_{ac}$ and the $AX62_{ac}$ alloys. The C36 Laves phases exhibits the same anodic dissolution tendency in both alloys. The C15 Laves phase within the $AX62_{ht}$ alloy in Fig. 9c) is entirely dissolved. The C14 Laves phase within the $AX44_{ac}$ alloy in Fig. 9d) reveals a ~30–50 nm thick hydroxide layer, while the adjacent α-solid solution exhibits a significant thicker hydroxide layer. Therefore, the C14 Laves phase acts as the cathode in the micro-galvanic corrosion with the adjacent α-solid solution under alkaline immersion conditions.

4. Discussion

4.1. Microstructure of Mg-Al-Ca alloys

The microstructures of the Mg-Al-Ca alloys investigated in our study agree with the structural characteristics reported in previous experimental [25-27] and theoretical studies [23,24], regarding the inherent phases, the corresponding phase fractions and their dependence on the nominal Ca/Al ratio. Furthermore, nm-scale Mg-rich precipitates were iden-

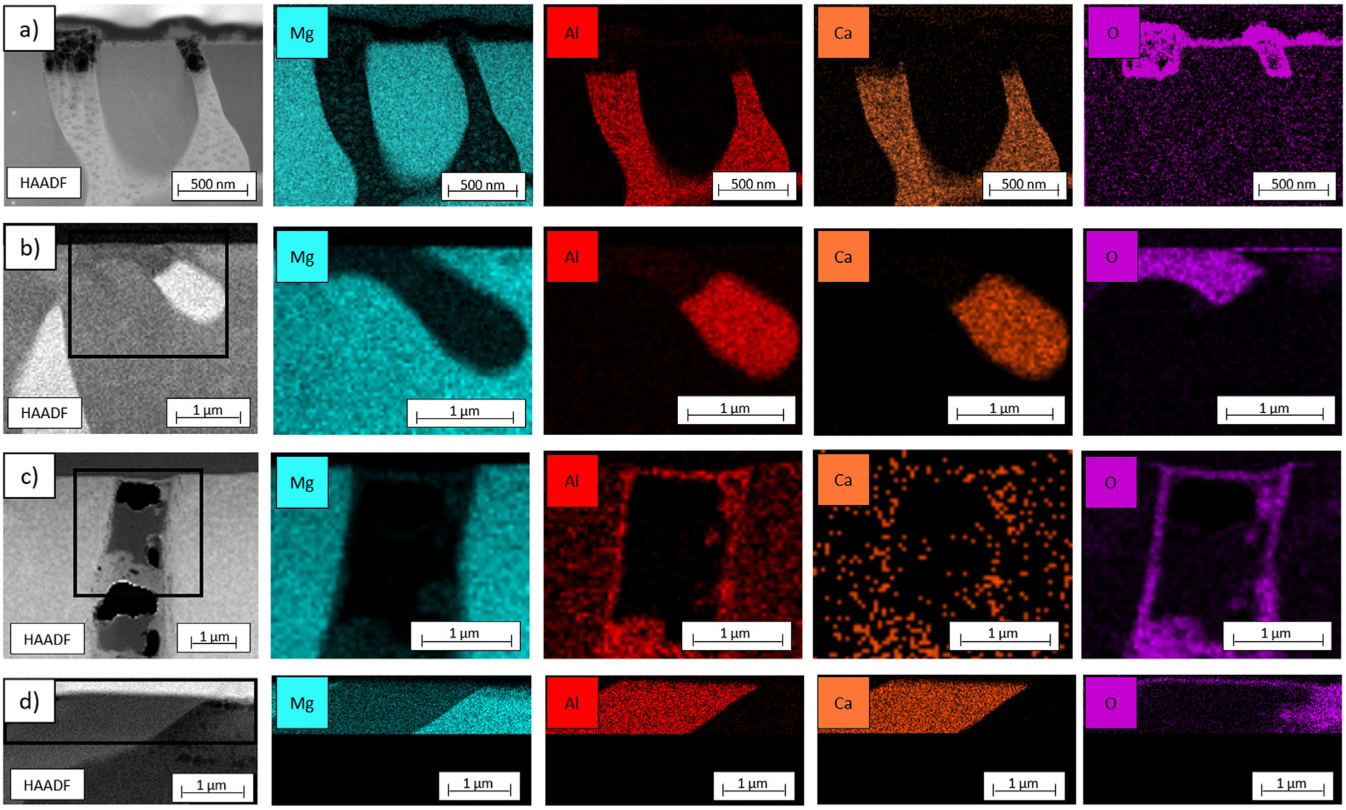

Fig. 9. STEM-EDS analysis of a) a C36 Laves phase in the AX53$_{ac}$ alloy, b) a C36 Laves phase in the AX62$_{ac}$ alloy, c) a C15 Laves phase in the AX62$_{ht}$ alloy and d) a C14 Laves phase in AX44$_{ac}$ alloy after an immersion time of 60 min in a KOH electrolyte (pH=11.5 ± 0.1).

tified within the C36 Laves phases in the AX54$_{ac}$ and the AX62$_{ac}$ alloys. The Mg-rich precipitates might form during the cooling process, due to a decreasing Mg solubility. Moreover, planar µm-scale Mg-rich precipitates were identified within the C36 and the C14 Laves phases in the AX44$_{ht}$ alloy. These planar µm-scale Mg-rich precipitates were exclusively observed after the heat treatment and might form during the C14 to C36 Laves phase solid-state transformation. The solid-state transformation initiates at the C14/α-solid solution interface via Al diffusion from the α-solid solution. The solid-state transformation further proceeds along this interface and encloses the C14 Laves phase in 3D. However, the Mg concentration within the enclosed C14 Laves phase equals c_{Mg}=47 at.%, while c_{Mg}=17 at.% was determined for the C36 Laves phase. Thus, the excess Mg atoms precipitate as the planar µm-scale Mg-rich precipitates, due to a restricted Mg diffusion through the C36 Laves phase.

4.2. Hydroxides and electrochemical phase stability

The hydroxide on the α-solid solution comprises an inner $Mg(OH)_{2\_dense}$ and a porous flake-like $Mg(OH)_{2\_flake}$ layer. While $Mg(OH)_{2\_flake}$ precipitates from the electrolyte [36], the $Mg(OH)_{2\_dense}$ layer is thermodynamically stable [42] and causes the observed passive behavior. Furthermore, Al enriched $Mg/Mg(OH)_{2\_dense}$ and $Mg(OH)_{2\_dense}/Mg(OH)_{2\_flake}$ interfaces were observed. However, the Al concentration within the α-solid solution is below the reported threshold (c_{Al}=4 wt.%) [38], leading to a minor effect on the electrochemical corrosion resistance. Similar Ca concentrations were determined within the α-solid solution [18]. Thus, Ca incorporation in the hydroxide is excluded as the underlying mechanism for the different corrosion resistances [40]. The observed electrochemical activities of the Laves phases contradict the cathodic C15 and C36 and the anodic C14 Laves phase character reported in neutral electrolytes [56,57,60,63,64]. The difference arises as a consequence of the formed stable $Mg(OH)_{2\_dense}$ layer, which significantly reduces the Mg dissolution [41]. Thus, the C15 and the C36 Laves phase dissolve as the anodes within the micro-galvanic coupling, which induces an ion saturation within the electrolyte in the surface cavities. Corrosion products form and restrict the mass transport, which subsequently induces the onset of the capacitive LF-loops in the EIS measurements. The AX53$_{ht}$ and the AX62$_{ht}$ alloys exhibit the largest surface cavities and corrosion product layers and therefore exhibit pronounced LF-loops. The molar Al/(Mg+Al) ratio equals ~95%, ~70%, ~35% and ~5% for the C15, the C36, the C14 Laves phases and the α-solid solution, respectively. The C15 and the C36 Laves phases correspond to Al-based systems and exhibit an active dissolution under alkaline immersion conditions [42]. The chemical composition of the C14 Laves phase and the α-solid solution correspond to a Mg-based system and form a passive $Mg(OH)_{2\_dense}$ hydroxide layer [42].

The Mg dissolution through the $Mg(OH)_{2\_dense}$ layer on the C14 Laves phase is reduced due to the increased Al content (c_{Al}>4 wt.%) [38]. Thus, the C14 Laves phase reveals a cathodic behavior. Beside the electrochemical phase stability, the corresponding phase fractions and the 3D phase morphology determine the global corrosion resistance of Mg-Al-Ca alloys.

4.3. Electrochemical corrosion mechanisms of Mg-Al-Ca alloys

The electrochemical corrosion mechanism of Mg-Al-Ca alloys is dominated by the micro-galvanic induced dissolution of the α-solid solution for a predominant C14 Laves phase within the microstructure. Therefore, the continuous 3D C14 Laves phase in the $AX44_{ac}$ alloy causes a constant high $i_{Mg,Ca}$ and an overall low corrosion resistance. A potential barrier effect is ineffective for minor penetration depths in the range of $l_{pd}\sim1$–2 µm. For Mg-Al-Ca alloys with a predominant C15 Laves phase within the microstructure, the anodic C15 Laves phase dissolution causes both the initial high $i_{Al,Ca}$ and the low OCP values. Thereafter, spherical 3D C15 particles dissolve rapidly, while the α-solid solution shows a significantly reduced dissolution tendency. Thus, a reduced C15/electrolyte interface emerges, that causes the gradual $i_{Al,Ca}$ decay and the increased OCP with an increasing immersion time. Therefore, the large dispersed C15 particle volume in the $AX53_{ht}$ alloy governs the observed low macroscopic corrosion resistance within the investigated immersion time compared to the $AX62_{ht}$ alloy, characterized by a reduced C15 Laves phase volume fraction (Table 3). However, the C15 Laves phases are not entirely dissolved towards the final immersion time, as no constant OCP is obtained. The C36 Laves phase instead exhibits a reduced dissolution tendency compared to the C15 Laves phase. This effect arises either due to a decreased molar Al/(Mg+Al) ratio or due to the inherent nm-scale Mg-rich precipitates. The nm-scale Mg-rich precipitates might form a local stable passive layer under alkaline immersion conditions and subsequently reduce the dissolution of the C36 Laves phase. Thus, the $AX53_{ac}$ alloy with exclusively C36 Laves phase within the microstructure exhibits the overall highest electrochemical corrosion resistance. The effect of the µm-scale planar Mg-rich precipitates within the C14 Laves phase on the macroscopic corrosion resistance is neglectable within the $AX44_{ht}$ alloy, as the C14 phases do not preferentially dissolve in the alkaline electrolyte.

4.4. Heat treatment induced effects on the electrochemical corrosion resistance

After the electrochemical phase activity and the electrochemical corrosion mechanisms of Mg-Al-Ca alloys were discussed, the heat treatment induced effects on the overall corrosion rate are derived. The heat treatment of the $AX44_{ac}$ alloy causes a C14 to C36 Laves phase solid-state transformation, leading to a predominant C36 Laves phase within the microstructure. While the continuous C14 Laves phase skeleton within the $AX44_{ac}$ alloy causes a constant micro-galvanic induced α-solid solution dissolution, the C36 Laves phase preferentially dissolves and acts as a sacrificial anode. This structural modification leads to a decrease of the corrosion current density in the range of ~80 % for the $AX44_{ht}$ alloy. However, the heat treatment of the $AX53_{ac}$ alloy significantly increases the corrosion rate within the investigated immersion time. The microstructural modification from a continuous C36 Laves phase network to 3D spherical dispersed C15 Laves phases causes a local C15 Laves phase dissolution, which increases the overall corrosion current density of the $AX53_{ht}$ alloy by a factor of 11 after 60 min immersion. The dispersed C15 Laves phases are not entirely dissolved towards the final immersion time. Thus, the corrosion rate will further decrease with progressing time, until the near-surface C15 Laves phases are entirely dissolved. The corrosion current density of the $AX62_{ac}$ alloy slightly decreases towards the final immersion time after the conducted heat treatment. While the C36 Laves phase in the $AX62_{ac}$ alloy causes a comparable high corrosion resistance, the local dissolution of the remaining near-surface C15 Laves phases in the $AX62_{ac}$ alloy still increases the corrosion current density after the final immersion time.

5. Conclusion

The microstructure of three different Mg-Al-Ca alloys in the as cast and in a heat-treated condition was investigated regarding the 2D and 3D Laves phase morphology as well as different nm-scale Mg-rich precipitates. Furthermore, the electrochemical corrosion resistance and the underlying corrosion mechanisms were analyzed in an alkaline electrolyte (pH=11.5 ± 0.1). The subsequent main results are derived:

- Mg-rich nm-scale precipitates were identified to exist within the C36 Laves phase of the $AX53_{ac}$ and the $AX62_{ac}$ alloys. The heat treatment induces a C14 to C36 solid-state transformation in the AX44 alloy causing the precipitation of planar µm-scale Mg-rich precipitates.
- A new electrochemical activity sequence (C15>C36>α-solid solution>C14) was observed under alkaline immersion conditions as a consequence of a stable $Mg(OH)_{2\_dense}$ layer formation on the α-solid solution.
- Large C15 Laves phase particles and an increasing phase fraction decrease the initial corrosion resistance, while small and dispersed C15 Laves phase particles increase the corrosion resistance of Mg-Al-Ca alloys with increasing immersion time.
- The C36 Laves phases show decreased dissolution kinetics compared to the C15 Laves phase. This effect might arise either due to a decreased molar Al/(Mg+Al) ratio or due to a local passive layer formation on the inherent nm-scale Mg-rich precipitates.
- An interconnected C14 Laves phase skeleton acts as the cathode in the micro-galvanic coupling with the adjacent α-solid solution and reduces the corrosion resistance of Mg-Al-Ca alloys.

Declaration of competing interest

The authors declare that they have no known competing financial interests or personal relationships that could have appeared to influence the work reported in this paper.

CRediT authorship contribution statement

Markus Felten: Writing – review & editing, Writing – original draft, Visualization, Validation, Methodology, Investigation, Formal analysis, Conceptualization. **Veronika Chaineux:** Writing – review & editing, Investigation, Conceptualization. **Siyuan Zhang:** Writing – review & editing, Investigation. **Ali Tehranchi:** Writing – review & editing. **Tilmann Hickel:** Writing – review & editing, Funding acquisition. **Christina Scheu:** Writing – review & editing, Funding acquisition, Conceptualization. **Joshua Spille:** Writing – review & editing, Investigation, Formal analysis. **Marta Lipińska-Chwałek:** Writing – review & editing, Investigation, Formal analysis. **Joachim Mayer:** Writing – review & editing, Funding acquisition. **Benjamin Berkels:** Writing – review & editing, Funding acquisition. **Marcus Hans:** Writing – review & editing, Funding acquisition. **Imke Greving:** Writing – review & editing, Formal analysis. **Silja Flenner:** Writing – review & editing, Formal analysis. **Sandra Sefa:** Writing – review & editing, Formal analysis. **Daniela Zander:** Writing – review & editing, Project administration, Funding acquisition.

Acknowledgements

The authors gratefully acknowledge the financial support of the Deutsche Forschungsgemeinschaft (DFG) of the Collaborative Research Center (CRC) 1394 "Structural and Chemical Atomic Complexity - from defect phase diagrams to material properties" – project ID 409476157 and the Excellence Strategy of the Federal Government and the Länder project ID G:(DE-82)EXS-SF-OPSF596. Furthermore, the authors acknowledge Hauke Springer from the Institute of Metal Forming at RWTH Aachen University for providing the investigated material and Deborah Neuß from Materials Chemistry at RWTH Aachen University for the support during FIB preparation of cylinders for the TXM investigations.

References

[1] S. Jayasathyakawin, M. Ravichandran, N. Baskar, C.A. Chairman, R. Balasundaram, Mater. Today Proc. 27 (2020) 909–913, doi:10.1016/j.matpr.2020.01.255.
[2] A. Atrens, M. Liu, N.I.Z. Abidin, Mater. Sci. Eng., B 176 (2011) 1609–1636, doi:10.1016/j.mseb.2010.12.017.
[3] D. Mei, S.V. Lamaka, X. Lu, M.L. Zheludkevich, Corros. Sci. 171 (2020) 108722, doi:10.1016/j.corsci.2020.108722.
[4] J. Bai, Y. Yang, C. Wen, J. Chen, G. Zhou, B. Jiang, X. Peng, F. Pan, J. Magnesium Alloys (2023), doi:10.1016/j.jma.2023.09.015.
[5] S. Tekumalla, M. Gupta, Mater. Des. 113 (2017) 84–98, doi:10.1016/j.matdes.2016.09.103.
[6] S.S. Prasad, S. Prasad, K. Verma, R.K. Mishra, V. Kumar, S. Singh, J. Magnesium Alloys 10 (2022) 1–61, doi:10.1016/j.jma.2021.05.012.
[7] W. Wang, J. Liu, J. Chen, W. Zhang, C. Li, Z. Shi, N. Wang, Electrochim.Acta 470 (2023) 143352, doi:10.1016/j.electacta.2023.143352.
[8] M. Deng, D. Höche, S.V. Lamaka, D. Snihirova, M.L. Zheludkevich, J. Power Sources 396 (2018) 109–118, doi:10.1016/j.jpowsour.2018.05.090.
[9] F. Tong, S. Wei, X. Chen, W. Gao, J. Magnes. Alloys 9 (2021) 1861–1883, doi:10.1016/j.jma.2021.04.011.
[10] H. Miura, T. Maruoka, X. Yang, J.J. Jonas, Scr. Mater. 66 (2012) 49–51, doi:10.1016/j.scriptamat.2011.10.005.
[11] J. Peng, Z. Zhang, Z. Liu, Y. Li, P. Guo, W. Zhou, Y. Wu, Sci. Rep. 8 (2018) 4196, doi:10.1038/s41598-018-22344-3.
[12] F. Wang, T. Hu, Y. Zhang, W. Xiao, C. Ma, Mater. Sci. Eng., A 704 (2017) 57–65, doi:10.1016/j.msea.2017.07.060.
[13] Y. Yang, Y. Deng, R. Zhang, Y. Su, S. Liu, C.M. Gourlay, G. Zeng, Corros. Sci. 222 (2023) 111363, doi:10.1016/j.corsci.2023.111363.
[14] H. Feng, S. Liu, Y. Du, T. Lei, R. Zeng, T. Yuan, J. Alloys Compd. 695 (2017) 2330–2338, doi:10.1016/j.jallcom.2016.11.100.
[15] Q. Zou, Q. Le, X. Chen, Y. Jia, C. Ban, T. Wang, H. Wang, R. Guo, L. Ren, A. Atrens, Electrochim. Acta 401 (2022) 139372, doi:10.1016/j.electacta.2021.139372.
[16] B. Mingo, M. Mohedano, C. Blawert, R. Del Olmo, N. Hort, R. Arrabal, J. Alloys Compd. 811 (2019) 151992, doi:10.1016/j.jallcom.2019.151992.
[17] M. Zubair, S. Sandlöbes-Haut, R. Pei, M.A. Wollenweber, L. Berners, C.F. Kusche, C. Liu, F. Roters, J.S.-L. Gibson, S. Korte-Kerzel, J. Mater. Res. (2023) 1–15, doi:10.1557/s43578-023-01082-x.
[18] M. Zubair, M. Felten, B. Hallstedt, M.V. Paredes, L. Abdellaoui, R.B. Villoro, M. Lipinska-Chwalek, N. Ayeb, H. Springer, J. Mayer, B. Berkels, D. Zander, S. Korte-Kerzel, C. Scheu, S. Zhang, Mater. Des. 225 (2023) 111470, doi:10.1016/j.matdes.2022.111470.
[19] M. Zubair, S. Sandlöbes-Haut, M. Lipińska-Chwałek, M. Wollenweber, C. Zehnder, J. Mayer, J.-L. Gibson, S. Korte-Kerzel, Mater. Des. 210 (2021) 110113, doi:10.1016/j.matdes.2021.110113.
[20] M. Zubair, S. Sandlöbes-Haut, M.A. Wollenweber, K. Bugelnig, C.F. Kusche, G. Requena, S. Korte-Kerzel, Mater. Sci. Eng., A 767 (2019) 138414, doi:10.1016/j.msea.2019.138414.
[21] M. Zubair, S. Sandlöbes, M. Wollenweber, C.F. Kusche, W. Hildebrandt, C. Broeckmann, S. Korte-Kerzel, Mater. Sci. Eng., A 756 (2019) 272–283, doi:10.1016/j.msea.2019.04.048.
[22] D. Amberger, P. Eisenlohr, M. Göken, Acta Mater. 60 (2012) 2277–2289, doi:10.1016/j.actamat.2012.01.017.
[23] B. Hallstedt, M. Noori, Calphad 82 (2023) 102577, doi:10.1016/j.calphad.2023.102577.
[24] A. Janz, J. Gröbner, H. Cao, J. Zhu, Y. Chang, R. Schmid-Fetzer, Acta Mater. 57 (2009) 682–694, doi:10.1016/j.actamat.2008.10.037.
[25] A. Suzuki, N.D. Saddock, J.W. Jones, T.M. Pollock, Metall. Mater. Trans. A 37 (2006) 975–983, doi:10.1007/s11661-006-0070-6.
[26] S. Sanyal, M. Paliwal, T.K. Bandyopadhyay, S. Mandal, Mater Sci. Eng., A 800 (2021) 140322, doi:10.1016/j.msea.2020.140322.
[27] Z. Li, X. Zhang, M. Zheng, X. Qiao, K. Wu, C. Xu, S. Kamado, Mater. Sci. Eng., A 682 (2017) 423–432, doi:10.1016/j.msea.2016.11.026.
[28] A. Atrens, G.L. Song, M. Liu, Z. Shi, F. Cao, M.S. Dargusch, Adv. Eng. Mater. 17 (2015) 400–453, doi:10.1002/adem.201400434.
[29] A. Atrens, G.-L. Song, Z. Shi, A. Soltan, S. Johnston, M. Dargusch, Encycl. Interfacial Chem. (2018) 515–534, doi:10.1016/B978-0-12-409547-2.13426-2.
[30] G. Song, A. Atrens, Adv. Eng. Mater. 5 (2003) 837–858, doi:10.1002/adem.200310405.
[31] M. Felten, J. Nowak, O. Beyss, P. Grünewald, C. Motz, D. Zander, Corros. Sci. 212 (2023) 110925, doi:10.1016/j.corsci.2022.110925.
[32] D. Neuß, I.E. McCarroll, S. Zhang, E. Woods, W.J. Delis, L. Tanure, H. Springer, S. Sandlöbes, J. Yang, M. Todorova, D. Zander, C. Scheu, J.M. Schneider, M. Hans, Corros. Sci. 227 (2024) 111776, doi:10.1016/j.corsci.2023.111776.
[33] M. Esmaily, J. Svensson, S. Fajardo, N. Birbilis, G. Frankel, S. Virtanen, R. Arrabal, S. Thomas, L. Johansson, Prog. in Mater. Sci. 89 (2017) 92–193, doi:10.1016/j.pmatsci.2017.04.011.
[34] S. Splinter, N. McIntyre, W. Lennard, K. Griffiths, G. Palumbo, Surf. Sci. 292 (1993) 130–144, doi:10.1016/0039-6028(93)90396-2.

[35] K. Refson, R.A. Wogelius, D.G. Fraser, M.C. Payne, M.H. Lee, V. Milman, Phys. Rev. B 52 (1995) 10823, doi:10.1103/PhysRevB.52.10823.

[36] J.H. Nordlien, S. Ono, N. Masuko, K. NişancioĞlu, J. Electrochem. Soc. 142 (1995) 3320, doi:10.1149/1.2049981.

[37] M. Taheri, R. Phillips, J. Kish, G. Botton, Corros. Sci. 59 (2012) 222–228, doi:10.1016/j.corsci.2012.03.001.

[38] J.H. Nordlien, K. NişancioĞu, S. Ono, N. Masuko, J. Electrochem. Soc. 143 (1996) 2564, doi:10.1149/1.1837048.

[39] J. Yang, K.S. Kumar, M. Todorova, J. Neugebauer, Phys. Rev. Mater. 7 (2023) 095802, doi:10.1103/PhysRevMaterials.7.095802.

[40] M. Deng, L. Wang, D. Höche, S.V. Lamaka, C. Wang, D. Snihirova, Y. Jin, Y. Zhang, M.L. Zheludkevich, Mater. Horiz. 8 (2021) 589–596, doi:10.1039/D0MH01380C.

[41] M. Felten, R. Changizi, C. Scheu, M. Bruns, M. Strebl, S. Virtanen, D. Zander, Electrochem. Commun. 153 (2023) 107529, doi:10.1016/j.elecom.2023.107529.

[42] M. Pourbaix, Atlas of Electrochemical Equilibria in Aqueous Solutions, NACE, 1966.

[43] S. Lebouil, O. Gharbi, P. Volovitch, K. Ogle, Corrosion 71 (2015) 234–241, doi:10.5006/1459.

[44] J. Światowska, P. Volovitch, K. Ogle, Corros. Sci. 52 (2010) 2372–2378, doi:10.1016/j.corsci.2010.02.038.

[45] B. Dou, X. Li, J. Han, N. Birbilis, K. Ogle, Corros. Sci. 217 (2023) 111095, doi:10.1016/j.corsci.2023.111095.

[46] S. Lebouil, A. Duboin, F. Monti, P. Tabeling, P. Volovitch, K. Ogle, Electrochim. Acta 124 (2014) 176–182, doi:10.1016/j.electacta.2013.07.131.

[47] S. Fajardo, J. Bosch, G.S. Frankel, Corros. Sci. 146 (2019) 163–171, doi:10.1016/j.corsci.2018.10.039.

[48] A.D. Gabbardo, G. Frankel, Corros. Sci. 164 (2020) 108321, doi:10.1016/j.corsci.2019.108321.

[49] G.S. Frankel, A. Samaniego, N. Birbilis, Corros. Sci. 70 (2013) 104–111, doi:10.1016/j.corsci.2013.01.017.

[50] C. Wang, D. Mei, G. Wiese, L. Wang, M. Deng, S.V. Lamaka, M.L. Zheludkevich, NPJ Mater. Degrad. 4 (2020) 42, doi:10.1038/s41529-020-00146-1.

[51] C. Wang, W. Xu, D. Höche, M.L. Zheludkevich, S.V. Lamaka, J. Magnesium Alloys 11 (2023) 100–109, doi:10.1016/j.jma.2022.09.031.

[52] M.-F. Ng, D.J. Blackwood, H. Jin, T.L. Tan, J.Electrochem. Soc. 170 (2023) 071501, doi:10.1149/1945-7111/ace243.

[53] O. Lunder, J. Lein, T.K. Aune, K. Nisancioglu, Corrosion 45 (1989) 741–748, doi:10.5006/1.3585029.

[54] K. Kadali, D. Dubey, R. Sarvesha, H. Kancharla, J. Jain, K. Mondal, S.S. Singh, JOM 71 (2019) 2209–2218, doi:10.1007/s11837-019-03470-3.

[55] C. Ubeda, G. Garces, P. Adeva, I. Llorente, G. Frankel, S. Fajardo, Corros. Sci. 165 (2020) 108384, doi:10.1016/j.corsci.2019.108384.

[56] E. Dabah, G. Ben-Hamu, V. Lisitsyn, D. Eliezer, K.S. Shin, J. Mater. Sci. 45 (2010) 3007–3015, doi:10.1007/s10853-010-4302-1.

[57] P.-p. Wu, F.-j. Xu, K.-k. Deng, F.-y. Han, Z.-z. Zhang, R. Gao, Corros. Sci. 127 (2017) 280–290, doi:10.1016/j.corsci.2017.08.014.

[58] G.L. Song, A. Atrens, Adv. Eng. Mater. 1 (1999) 11–33. doi:10.1002/(SICI)1527-2648(199909)1:1⟨11::AID-ADEM11⟩3.0.CO;2-N.

[59] G. Song, A. Atrens, X. Wu, B. Zhang, Corros. Sci. 40 (1998) 1769–1791, doi:10.1016/S0010-938X(98)00078-X.

[60] J. Yang, J. Peng, E.A. Nyberg, F.-s. Pan, Appl. Surf. Sci. 369 (2016) 92–100, doi:10.1016/j.apsusc.2016.01.283.

[61] C. Shuai, C. He, L. Xu, Q. Li, T. Chen, Y. Yang, S. Peng, Virtual Phys. Prototyping 13 (2018) 292–300, doi:10.1080/17452759.2018.1479969.

[62] A. Bahmani, S. Arthanari, S.K. Sheon, J. Magnesium Alloys 8 (2020) 134–149, doi:10.1016/j.jma.2019.12.001.

[63] A. Bahmani, S. Arthanari, S.K. Seon, J. Magnesium Alloys 7 (2019) 38–46, doi:10.1016/j.jma.2018.11.004.

[64] S.-M. Baek, J.S. Kang, H.-J. Shin, C.D. Yim, B.S. You, H.-Y. Ha, S.S. Park, Corros. Sci. 118 (2017) 227–232, doi:10.1016/j.corsci.2017.01.022.

[65] D. Andre, M. Freund, U. Rehman, W. Delis, M. Felten, J. Nowak, C. Tian, M. Zubair, L. Tanure, L. Abdellaoui, H. Springer, J.P. Best, D. Zander, G. Dehm, S. Sandlöbes-Haut, S. Korte-Kerzel, Mater. Charact. 192 (2022) 112187, doi:10.1016/j.matchar.2022.112187.

[66] M. Felten, J. Nowak, P. Grünewald, F. Schäfer, C. Motz, D. Zander, The role of native oxides on the corrosion mechanism of laves phases in Mg–Al–Ca composites, in: Magnesium 2021, Springer, 2021, pp. 217–225.

[67] K. Bredies, D. Lorenz, Mathematical Image Processing, Springer, 2018.

[68] A. Kovács, R. Schierholz, K. Tillmann, JLSRF 2 (2016) A43 -A43, doi:10.17815/jlsrf-2-68.

[69] S. Zhang, C. Scheu, Microscopy 67 (2018) i133–i141, doi:10.1093/jmicro/dfx091.

[70] S. Zhang, I. Ahmet, S.-H. Kim, O. Kasian, A.M. Mingers, P. Schnell, M. Kölbach, J. Lim, A. Fischer, K.J. Mayrhofer, S. Cherevko, B. Gault, R. Krol, C. Scheu, ACS Appl. Energy. Mater. 3 (2020) 9523–9527, doi:10.1021/acsaem.0c01904.

[71] S. Flenner, M. Storm, A. Kubec, E. Longo, F. Döring, D.M. Pelt, C. David, M. Müller, I. Greving, J. Synchrotron Radiat. 27 (2020) 1339–1346, doi:10.1107/S1600577520007407/mo5217sup1.pdf.

[72] D. Gürsoy, F. De Carlo, X. Xiao, C. Jacobsen, J. Synchrotron Radiat 21 (2014) 1188–1193, doi:10.1107/S1600577514013939.

[73] S. Bruns, S.L.S. Stipp, H.O. Sørensen, Water. Resour. Res. 105 (2017) 96–107, doi:10.1016/j.advwatres.2017.04.020.

[74] D. Zander, P. Zaslansky, N.A. Zumdick, M. Felten, C. Schnatterer, V.F. Chaineux, J.U. Hammel, M. Storm, F. Wilde, C. Fleck, Adv. Eng. Mater. 23 (2021) 2100157, doi:10.1002/adem.202100157.

[75] G. Baril, C. Blanc, N. Pébère, J. Electrochem. Soc. 148 (2001) B489, doi:10.1149/1.1415722.

[76] G. Baril, N. Pebere, Corros. Sci. 43 (2001) 471–484, doi:10.1016/S0010-938X(00)00095-0.

[77] G. Makar, J. Kruger, J. Electrochem. Soc. 137 (1990) 414, doi:10.1149/1.2086455.

[78] L. Wang, D. Snihirova, M. Deng, C. Wang, B. Vaghefinazari, G. Wiese, M. Langridge, D. Höche, S.V. Lamaka, M.L. Zheludkevich, Corros, Sci. 187 (2021) 109501, doi:10.1016/j.corsci.2021.109501.

[79] B. Hirschorn, M.E. Orazem, B. Tribollet, V. Vivier, I. Frateur, M. Musiani, J. Electrochem. Soc. 157 (2010) C458, doi:10.1149/1.3499565.

[80] S. Mathieu, C. Rapin, J. Steinmetz, P. Steinmetz, Corros. Sci. 45 (2003) 2741–2755, doi:10.1016/S0010-938X(03)00109-4.

[81] M. Grimm, A. Lohmüller, R.F. Singer, S. Virtanen, Corros. Sci. 155 (2019) 195–208, doi:10.1016/j.corsci.2019.04.024.